A Multi-Inverter High-Power Wireless Power Transfer System With Wide ZVS Operation Range

Xin Liu, *Member, IEEE*, Fei Gao, *Member, IEEE*, Yiming Zhang, *Senior Member, IEEE*, Muhammad Mansoor Khan, *Member, IEEE*, Yun Zhang, *Senior Member, IEEE*, Tianfeng Wang, and Daniel J. Rogers, *Senior Member, IEEE*

***Abstract*—Conventional high-power wireless power transfer (WPT) systems that are required to deliver power over a wide operating range suffer from issues like hard switching, poor current sharing, and unwanted cross-coupling issues. This article proposes a new resonant inductor integrated-transformer-based multi-inverter to improve the WPT power rating without compromising performance. Viable modulation schemes of the proposed system are analyzed, and a hybrid modulation scheme is proposed for wide-range power regulation. To further investigate the feasibility of the proposed system, the power transfer capacity, current sharing among multiple inverters, and the soft switching regions are studied. A 14-kW *LCC–LCC* WPT experimental system with three parallel inverters is built, which achieves 93.5% efficiency, demonstrating the high performance of the proposed system. This article is accompanied by a video demonstrating these experiments.**

***Index Terms*—Hybrid modulation, multi-inverter (MI), wireless power transfer (WPT).**

I. Introduction

WIRELESS power transfer (WPT) for electric vehicles (EVs) delivers power from the grid to the battery through magnetically coupled coils. This technique is very convenient for EV charging and is well suited for the fast-growing driverless technique.

With the development of battery and power electronics technologies, modern EVs are shifting to higher power ratings to improve their performance and range. The battery capacities of BYD Song Plus DMi and Tesla Model S are 18 and 40–80 kWh, respectively. Manufactures like Hongqi for their E-HS9 model and Porsche for the Taycan model have already reached 100 kWh [1]. Table I lists the charging hours of different battery packs, where the power rating of the WPT system increases from 3.7 to 22 kVA [2]. A higher power rating can obtain a desirable shorter charging time. In the widely used WPT designs like *LCC–LCC*, the system output power is proportional to the coupling coefficient of the coils [3]. However, the ground assembly (GA) and the vehicle assembly (VA) are physically separated, resulting in varying coupling coefficients ranging from 0.088 to 0.245 [2]. In addition, as a public facility, the GA is fixed and needs to be compatible with various EVs with different power ratings. Thus, the GA should have a high power transfer capability and a wide regulation range.

To increase the power transfer capability of the system, various topologies have been investigated, as shown in Fig. 1. Fig. 1(a) shows the first candidate for the high-power inverter by paralleling MOSFETs, or by using a semiconductor module [4].

TABLE I
Wireless Charging Hours of Different Batteries

Battery capacity	WPT1 3.7 kVA	WPT2 7.7 kVA	WPT3 11.1 kVA	WPT4 22 kVA
18 kWh	5.5 h	2.6 h	1.8 h	0.9 h
60 kWh	18.2 h	8.6 h	6 h	3 h
100 kWh	30.3 h	14.3 h	10 h	5 h

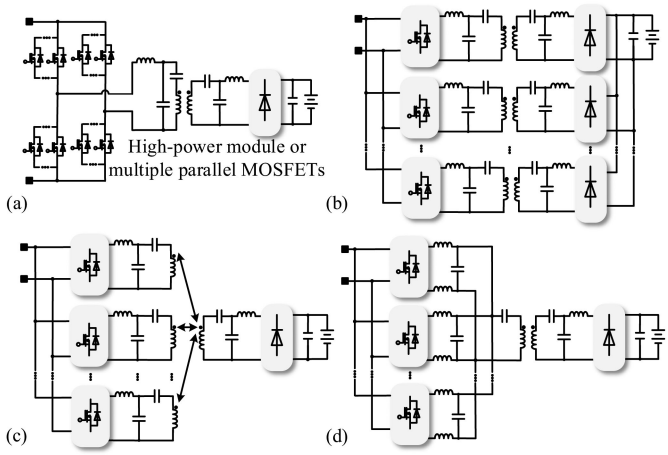

Fig. 1. Topology candidates for the high-power WPT systems. (a) Multi-MOSFET topology [4], [5]. (b) Multi-cell topology in [7]–[9]. (c) Multi-GA topology in [12] and [13]. (d) Multi-inverter topology in [14] and [15].

Manuscript received 11 May 2022; revised 29 June 2022; accepted 27 July 2022. Date of publication 2 August 2022; date of current version 6 September 2022. This work was supported by the Natural Science Foundation of Shanghai under Grant 22ZR1429800. Recommended for publication by Associate Editor S. Tian. *(Corresponding author: Fei Gao.)*

Xin Liu, Fei Gao, Muhammad Mansoor Khan, and Tianfeng Wang are with the Key Laboratory of Control of Power Transmission and Conversion, Ministry of Education, China, and the Department of Electrical Engineering, Shanghai Jiao Tong University, Shanghai 200240, China (e-mail: liu_xin@sjtu.edu.cn; fei.gao@sjtu.edu.cn; mansoor@sjtu.edu.cn; wangtf1992@sjtu.edu.cn).

Yiming Zhang is with the College of Electrical Engineering and Automation, Fuzhou University, Fuzhou 350108, China (e-mail: zym@fzu.edu.cn).

Yun Zhang is with the School of Electrical and Information Engineering, Tianjin University, Tianjin 300072, China (e-mail: zhangy@tju.edu.cn).

Daniel J. Rogers is with the Department of Engineering Science, University of Oxford, OX1 2JD Oxford, U.K. (e-mail: dan.rogers@eng.ox.ac.uk).

This article has supplementary material provided by the authors and color versions of one or more figures available at https://doi.org/10.1109/TPEL.2022.3195866.

Digital Object Identifier 10.1109/TPEL.2022.3195866

Since the power module is expensive and has the disadvantage of high gate inductances, which, in turn, leads to poor commutation [5], using parallel discrete MOSFETs is preferred. However, the parameter variation of different devices can bring about the current sharing issue [6], in which the MOSFET turned OFF at last will have to withstand all the switch-OFF currents. This, in turn, may cause damage to the device. In addition, it is difficult for the multi-MOSFET topology to achieve soft switching and a wide power regulation range simultaneously.

The multicell topology shown in Fig. 1(b) is used to reduce the current stress of semiconductors [7]–[9]. In [7], a 50-kW input-parallel output-parallel WPT system with three cells is presented with the dc–dc efficiency of 95.2%. Similar topologies can also be applied to input-parallel output-series, input-series output-parallel, and input-series output-series systems. This solution relies on a large VA due to the usage of multiple coupling coils, which is suitable for large vehicles like buses, trucks, or high-speed trains [10]. However, it is not feasible to utilize several receiving coils in the EVs for home use due to the limited space and cost.

To reduce the VA size, the multi-GA topology is shown in Fig. 1(c). In [11], a 50-kW three-phase WPT system with three transmitting coils was investigated. In [12], an input-series output-equivalent-parallel multi-GA topology was proposed for the series–series high-power WPT system, where a maximum dc–dc efficiency of 89.31% at 38.4 kW has been achieved. In [13], an input-parallel output-equivalent-parallel multi-GA topology was presented with a dc–dc efficiency of 92.6% at 12.5 kW. The voltage sharing in [12] and the current sharing in [13] are challenging. In addition, the multiple transmitters overlap with each other, which means there exists a strong cross-coupling effect among different transmitting coils.

A multi-inverter (MI) topology is shown in Fig. 1(d) which avoids the cross-coupling issue. In [14], this MI topology was applied to the dynamic charging scenario. In [15], MI topology was employed for the *LCC*-series circuit to reduce the power losses. The dc–dc efficiency was higher than 90% when the power ranges from 1.5 to 3 kW. However, additional *LC* circuits are needed, and the circulating currents among different inverters may increase. An MI topology with fewer components is desired to achieve higher efficiency and power density.

To achieve soft switching and adapt to power variations, additional circuits [16]–[19] and various modulation schemes [20]–[22] have been applied to the WPT system. In [16], primary and secondary dc–dc converters were used to regulate the input and output voltages. In [17], an auxiliary variable inductor was introduced to extend the zero-voltage switching (ZVS) region of the WPT system. In [23], a tuning capacitor control is applied to a 10-W series–series WPT system to obtain ZVS operation during constant voltage/constant current charging. In [18], soft switching was realized by dual-side 90° phase shift for the WPT system. In [19], a triple-phase-shift control strategy was proposed to achieve a wide ZVS operation range. However, additional components in [16] and [17] or active rectifiers in [18] and [19] increase the cost and reduce the power density of the system. To obtain a compact and cost-effective solution, several modulation schemes have been applied to the inverter, including phase shift control (PSC) [21], frequency shift control (FSC) [22], duty cycle control (DCC) [24], on-off keying (OOK) [25], etc. To ensure a stable magnetic field and reduce interferences, the operating frequency of the EV WPT system is usually fixed at 85.5 kHz [16], which means modulation methods such as FSC and OOK are not suitable in practice. Therefore, it is quite challenging to extend the power regulation range by only modulating the primary inverter at a fixed frequency.

To obtain a high-power, cost-effective, and compact WPT system, a resonant inductor integrated-transformer-based MI (RIIT-MI) WPT system is proposed in this article. It can overcome the abovementioned current sharing, cross-coupling, and soft switching issues. The main contributions of this article are following.

1) A modular RIIT-MI topology is proposed for the high-power WPT system which can eliminate the resonant inductor and achieve autonomous current sharing among multiple inverters.
2) A hybrid modulation scheme is proposed to obtain a wide dc–ac voltage gain.
3) The criterion for the wide ZVS operation range is achieved despite power variations.

The rest of this article is organized as follows. Section II presents the proposed RIIT-MI WPT system and analyzes the modulation schemes, including full-bridge mode with PSC (FB-PSC), half-bridge mode with DCC (HB-DCC), and by-pass control (BPC). The autonomous current sharing characteristic is also studied in this section. Section III investigates the power transfer capacity and proposes a new hybrid modulation scheme for the wide ZVS operation range. Section IV presents the experimental verification and Section V draws the conclusion.

II. Proposed RIIT-MI WPT System

Due to the robustness to load variation and high degrees of freedom in parameter design [3], the *LCC–LCC* topology has been adopted by many EV WPT manufacturers such as WiTricity, VIE, etc. Thus, the proposed RIIT-MI topology is first applied to the *LCC–LCC* WPT system. This section discusses the advantages and the modulation schemes of the proposed system.

A. Proposed Topology

The schematic of the proposed RIIT-MI WPT system is shown in Fig. 2. $V_{\rm bus}$ is the input dc-link voltage. $V_{\rm bat}$ and $I_{\rm bat}$ are the battery voltage and current, respectively. n is the number of the inverters which is determined by the power rating. S_{1i}–S_{4i} are the MOSFETs of #i inverter. $v_{\rm p1}$ and $i_{\rm inv}$ are the inverting voltage and current of #1 inverter. $v_{{\rm p}i}$ and $v_{{\rm s}i}$ are the primary and secondary voltages of #i RIIT and $i_{{\rm p}i}$ is the inverting current where $i = 2, \ldots, n$. $v_{\rm rec}$ and $i_{\rm rec}$ are the rectified voltage and current, respectively. The primary and secondary turns of #i RIIT are $n_{{\rm p}i}$ and $n_{{\rm s}i}$, and the turns ratio n_i is defined as

$$n_i = n_{{\rm p}i}/n_{{\rm s}i}. \tag{1}$$

$C_{\rm fga}$, $C_{\rm ga}$, $C_{\rm va}$, and $C_{\rm fva}$ are resonant compensation capacitors. $L_{\rm fva}$ is the filtering inductance of the VA. D_1–D_4 are the rectification diodes. Since the forward voltage of the SiC

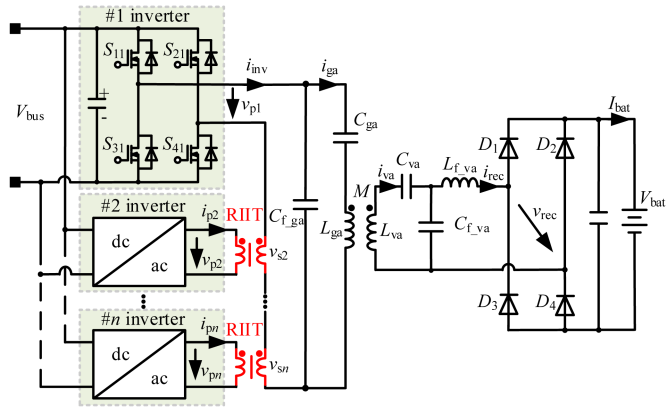

Fig. 2. Proposed RIIT-MI WPT system.

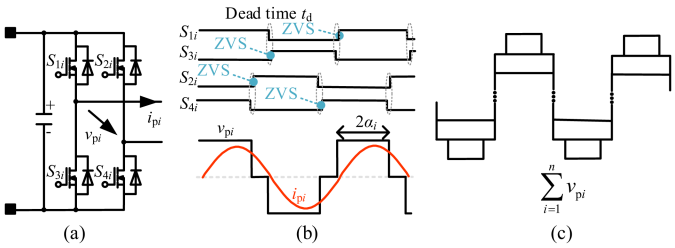

Fig. 3. FB-PSC scheme. (a) Circuit diagram. (b) Typical waveforms. (c) Sum of the inverting voltages.

diode has a positive temperature coefficient, more diodes can be connected in parallel to increase the power rating of the VA. $L_{\rm ga}$ and $L_{\rm va}$ are the inductances of the coupling coils. The relationship between the coupling coefficient k and mutual inductance M can be defined as

$$M = k\sqrt{L_{\rm ga}L_{\rm va}}. \tag{2}$$

It is clearly seen from Fig. 2 that the proposed RIIT-MI topology has several advantages. First, the power rating can be easily improved by increasing the number of modular inverters due to the dc-link parallel ac-link series (DPAS) characteristic. Second, the conventional resonant inductor of the *LCC* circuit is replaced by the leakage inductance of the RIITs, which helps to increase the power density. Third, the resonant capacitors $C_{\rm fga}$ and $C_{\rm ga}$ block the dc bias voltage. Note that #1 inverter is directly connected to the resonant tank. This eliminates one RIIT and means that asymmetric modulation such as the HB-DCC scheme can be applied to the system.

B. Modulation Analysis

The EV WPT system needs to provide a wide-range power supply for various EVs with different power ratings. Although applying multiple modulation methods to the proposed RIIT-MI topology increases the control complexity, it can extend the power regulation range and optimize the switching conditions of the inverters. Thus, various feasible continuous pulsewidth modulation schemes are studied here.

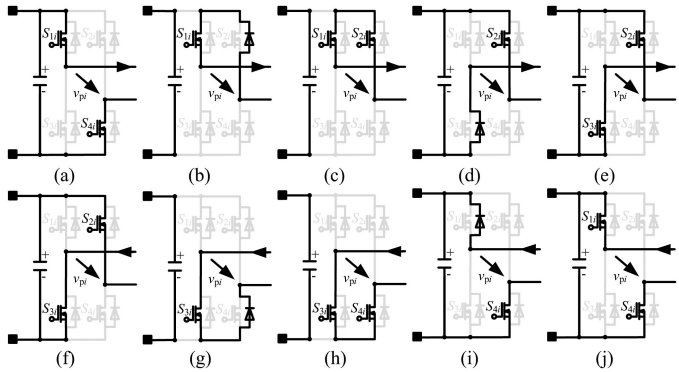

Fig. 4. Operating modes of the FB-PSC scheme.

1) FB-PSC Scheme: Fig. 3 shows the schematic and typical waveforms of the FB-PSC scheme. α_i is the phase angle of the inverting voltage. To obtain the ZVS operation, S_{1i} should turn ON when $i_{\rm inv}$ is negative as shown in Fig. 3(b). It means that α_i should be relatively large such as 90°. When applying multiple inverters, the power capacity increases with the sum of the inverting voltages as shown in Fig. 3(c).

Fig. 4 shows the 10 operating modes of the FB-PSC scheme whose typical waveform is presented in Fig. 3(b) where $t_{\rm d}$ is the dead time. The current flows through the diode before the MOSFET turns ON. It can be inferred that all MOSFETs can achieve ZVS switching on, which benefits efficiency improvement.

The fundamental harmonic approximation (FHA) is widely used in the WPT system due to its strong filtering effect. The power transfer mainly depends on the fundamental voltages. The rms values of the fundamental harmonic of each inverting voltage can be expressed as [21]

$$V_{{\rm p}i} = 2\sqrt{2}V_{\rm bus}\sin\alpha_i/\pi. \tag{3}$$

Since ZVS is obtained, the power loss of #*i* inverter at FB-PSC scheme $P_{{\rm psc\_}i}$ is:

$$P_{\rm PSC\_i} = \begin{cases} 2I_{\rm inv}^2 R_{\rm dson} + 4fE_{\rm off}, i = 1 \\ 2I_{\rm inv}^2 R_{\rm dson}/n_i^2 + 4fE_{\rm off}, i \geq 2 \end{cases} \tag{4}$$

where $E_{\rm off}$ is the turn-off energy that is strongly related to the switching-OFF current. The use of SiC MOSFETs instead of Si MOSFETs will reduce $E_{\rm off}$ significantly.

2) HB-DCC Scheme: When α_i decreases to a certain level, hard switching occurs. The HB-DCC scheme has a smaller voltage gain than the FB-PSC scheme. In addition, it is easier to achieve soft switching. Thus, the HB-DCC scheme is introduced to #1 inverter when a small voltage gain is required, whose typical waveform is shown in Fig. 5. The upper-side MOSFET S_{21} remains OFF, whereas the lower-side MOSFET S_{41} remains ON. $v_{\rm p1}$ leads $i_{\rm inv}$ as shown in Fig. 5(b) and the ZVS operation is realized. A small voltage can be added to the total inverting voltage as shown in Fig. 5(c).

Fig. 6 shows the six operating modes of the HB-DCC scheme. Although S_{11} and S_{31} are still complementary to each other, the duty cycle of the gate signals is changed to regulate $v_{\rm p1}$ where the maximum duty cycle is 50%. By applying the Fourier analysis to

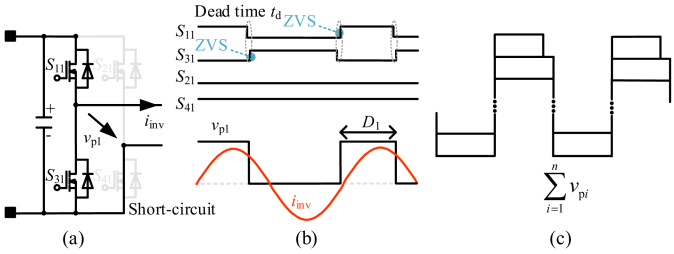

Fig. 5. HB-DCC scheme. (a) Circuit diagram. (b) Typical waveforms. (c) Sum of the inverting voltages.

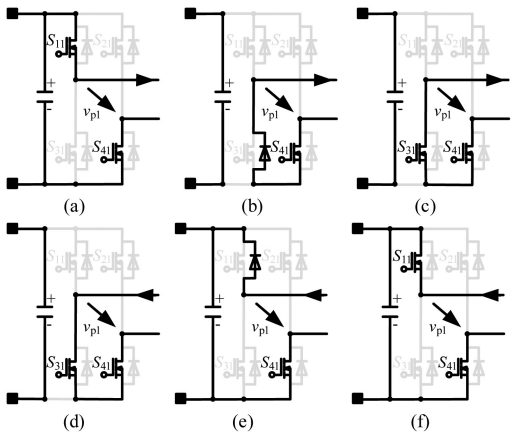

Fig. 6. Operating modes of the HB-DCC scheme.

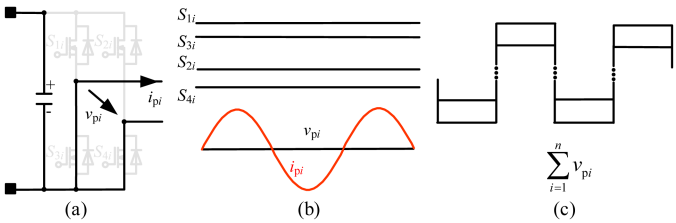

Fig. 7. BPC scheme. (a) Circuit diagram. (b) Typical waveforms. (c) Sum of the inverting voltages.

v_{p1} in Fig. 5(b), one can obtain the rms value of the fundamental voltage as [26]

$$V_{p1} = \sqrt{2} V_{bus} \sin(D_1 \pi)/\pi. \tag{5}$$

Only #1 inverter can operate at the HB-DCC scheme and the corresponding power loss P_{HB_1} is defined as

$$P_{HB\_1} = 2I_{inv}^2 R_{dson} + 2fE_{off}. \tag{6}$$

To balance the temperature rise of each MOSFET, the leading and lagging legs can work alternately.

3) BPC Scheme: Fig. 7 shows the schematic and typical waveforms of the BPC scheme. S_{1i} and S_{2i} remain OFF, whereas S_{3i} and S_{4i} remain ON. It should be mentioned that S_{2i} and S_{4i} can be conducted alternately to share the power losses between these MOSFETs. The dc–ac voltage gain decreases to zero. It can be regarded as a special case of the FB-PSC where α_i is 0°. The voltage across the transformer v_{pi} is nearly zero, which means the magnetic core loss of #*i* RIIT is reduced to zero. However, i_{inv} still flows through these transformers, and the power loss of #*i* inverter operating at the BPC scheme can be derived as

$$P_{BPC\_i} = \begin{cases} 2I_{inv}^2 R_{dson}, i = 1 \\ 2I_{inv}^2 R_{dson}/n_i^2, i \geq 2 \end{cases}. \tag{7}$$

C. Proposed Hybrid Modulation Scheme

A wide power regulation range is essential for the high-power WPT system. Although adding additional dc–dc converters can provide better flexibility, it increases the power losses and degrades the overall efficiency. Without additional dc–dc converters, V_{bus} is assumed to be unchanged due to the limited voltage regulation range of the front-end converter. The power regulation highly depends on the proposed RIIT-MI topology. Although all the inverters can use the same gate signals, hard switching occurs at light loading with a small α_i. A continuous hybrid modulation scheme is proposed here to provide a wide dc–ac voltage gain.

To avoid the dc bias voltage across the RIIT, only symmetrical FB-PSC and BPC schemes are applied to #2 $\sim$ #*n* inverters. However, #1 inverter can also operate at the HB-DCC scheme. According to (3) and (5), a generalized equivalent phase angle α_{1eq} for three schemes is defined as

$$\alpha_{1eq} = \begin{cases} \alpha_1, & \text{FB} - \text{PSC/BPC} \\ D_1\pi, & \text{HB} - \text{DCC} \end{cases}. \tag{8}$$

Thus, one can obtain the generalized expression of V_{p1}

$$V_{p1} = 2\sqrt{2} V_{bus} [0.25\text{sgn}(x) + 0.75] \sin \alpha_{1eq}/\pi \tag{9}$$

where the operating mode x is defined as

$$x = \begin{cases} 1, & \text{FB} - \text{PSC} \\ -1, & \text{HB} - \text{DCC} \end{cases}. \tag{10}$$

To obtain the maximum power transfer capacity, the inverting voltages are in phase with each other. By combining (3) and (9), one can obtain the generalized total inverting volage V_{inv} as

$$V_{inv} = 2\sqrt{2} \left([0.25\text{sgn}(x) + 0.75] \sin \alpha_{1eq} + \sum_{i=2}^{n} \sin \alpha_i / n_i \right) V_{bus}/\pi. \tag{11}$$

To quantify the voltage conversion capability, a dc–ac voltage gain $G_{dc\text{-}ac}$ is introduced as follows:

$$G_{dc-ac} = V_{inv}/V_{bus} = 2\sqrt{2} \left([0.25\text{sgn}(x) + 0.75] \sin \alpha_{1eq} + \sum_{i=2}^{n} \sin \alpha_i / n_i \right) /\pi. \tag{12}$$

The HB-DCC scheme is used to avoid the usage of a small α_i. When #1 inverter changes from the HB-DCC scheme with 50% duty cycle to the BPC scheme, #*i* inverter changes from the BPC scheme to the FB-PSC scheme. Since the value of the

TABLE II
OPERATING MODES OF ALL INVERTERS FOR DIFFERENT $G_{\mathrm{DC—AC}}$

Mode	# 1 inverter	# 2 inverter	…	# n-1 inverter	# n inverter	Voltage gain $G_{\mathrm{dc\text{-}ac}}$ ($n_i = 2$)
1	HB-DCC	BPC	…	BPC	BPC	$[0, \frac{\sqrt{2}}{\pi}]$
2	HB-DCC	$\alpha_2 = 90°$	…	BPC	BPC	$(\frac{\sqrt{2}}{\pi}, \frac{2\sqrt{2}}{\pi}]$
…	…	…	…	…	…	…
n-1	HB-DCC	$\alpha_2 = 90°$	…	$\alpha_{n-1} = 90°$	BPC	$(\frac{\sqrt{2}(n-2)}{\pi}, \frac{\sqrt{2}(n-1)}{\pi}]$
n	HB-DCC	$\alpha_2 = 90°$	…	$\alpha_{n-1} = 90°$	$\alpha_n = 90°$	$(\frac{\sqrt{2}(n-1)}{\pi}, \frac{\sqrt{2}n}{\pi}]$
n+1	FB-PSC	$\alpha_2 = 90°$	…	$\alpha_{n-1} = 90°$	$\alpha_n = 90°$	$(\frac{\sqrt{2}n}{\pi}, \frac{\sqrt{2}(n+1)}{\pi}]$

voltage gain should be continuously adjustable, one can obtain the minimum phase angle $\alpha_{i\_\min}$ as (13) according to (3) and (5)

$$\alpha_{i\,\min} = \arcsin(0.5n_i). \tag{13}$$

A smaller n_i corresponds to a greater power transfer capability of #i inverter. One can allocate the power of each inverter by using different turns ratios. To simplify the analysis, the turns ratios are set to be identical

$$n_2 = \cdots = n_n. \tag{14}$$

It is worth mentioning that there are two special cases of n_i. One is that n_i equals 1, indicating that all the currents flowing through the MOSFETs are identical. However, when $\alpha_{i\_\min}$ is 30° according to (13), soft switching is difficult to achieve by the FB-PSC scheme. The other case of interest is when n_i equals 2 where $\alpha_{i\_\min}$ is 90°. Although ZVS operation can be easily achieved, the current flowing through #1 inverter is twice that of the others. This requires using a MOSFET with a lower on-resistance (or two parallel MOSFETs) for #1 inverter.

Table II shows all possible operating modes of the system to achieve a continuous voltage gain $G_{\mathrm{dc\text{-}ac}}$. Since #1 inverter can work at the FB-PSC scheme or the BPC scheme, the number of total operating modes is n+1. The voltage gain intervals of v_{inv} can be divided into [0, 0.45), [0.45, 0.90), …, [0.45n, 0.45(n+1)] when $n_i = 2$. Although the proposed hybrid modulation scheme integrates multiple control strategies and variables which makes the system more complicated, it helps to obtain a wide range of voltage gain with ZVS operation.

To make it more intuitive, Fig. 8 shows the operating modes of each inverter at different voltage gains when using the proposed hybrid modulation scheme. Once $G_{\mathrm{dc\text{-}ac}}$ is determined according to the desired output power, the primary controller will set all the inverters at the corresponding mode. An example including all gate signals and typical inverting voltages is given, which corresponds to Mode 2 in Table II. #1, #2, and #3 ~ #n inverters operate at the HB-DCC scheme, the FB-PSC scheme with 90°, and the BPC scheme, respectively.

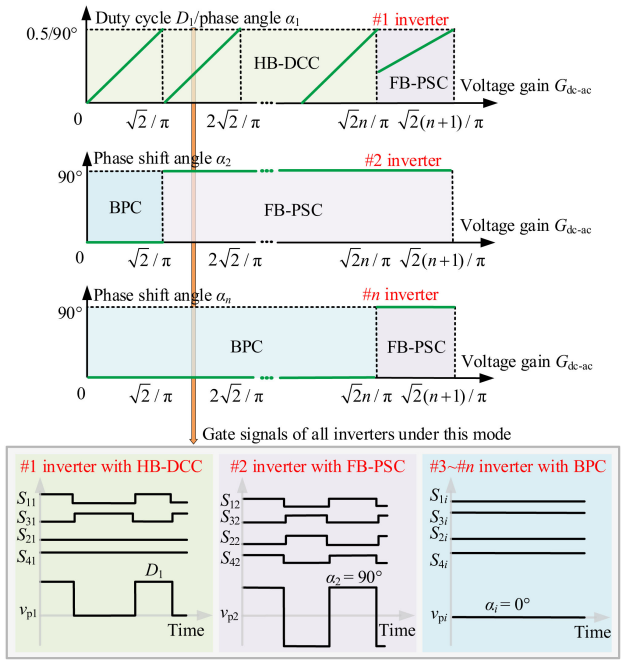

Fig. 8. Operating mode of each inverter at different voltage gain $G_{\mathrm{dc\text{-}ac}}$ when $n_i = 2$.

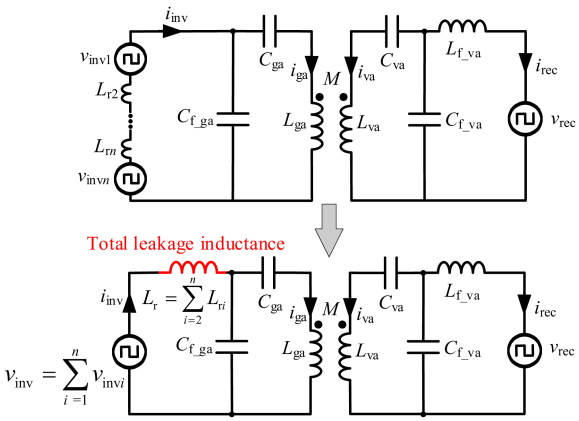

Fig. 9. Equivalent circuit of the proposed RIIT-MI LCC-LCC WPT system.

III. PERFORMANCE ANALYSIS

This section provides a detailed analysis of the proposed system including power transfer capacity, autonomous current sharing, and the ZVS operation range.

A. Power Transfer Capacity

The equivalent circuit of the proposed RIIT-MI LCC-LCC WPT system is shown in Fig. 9. According to (1), one can obtain the relationship between the primary and secondary voltages as

$$\mathbf{V_{invi}} = \mathbf{V_{pi}}/n_i. \tag{15}$$

The secondary windings of all RIITs are connected in series, and the conventional resonant inductor of the *LCC* topology is replaced by the total leakage inductance of the RIITs ($L_{\rm r}$). Thus, $\mathbf{V_{inv}}$ and $L_{\rm r}$ can be calculated as

$$\begin{aligned}\mathbf{V_{inv}}&=\mathbf{V_{inv}}_1+\mathbf{V_{inv}}_2+\ldots+\mathbf{V_{inv}}_n\\&=\sum_{i=1}^{n}\mathbf{V_{inv}}_i=\mathbf{V_{p}}_1+\sum_{i=2}^{n}\mathbf{V_{p}}_i/n_i\end{aligned}\tag{16}$$

$$L_{\rm r}=L_{\rm r}2+\cdots+L_{\rm r}n=\sum_{i=2}^{n}L_{{\rm r}i}.\tag{17}$$

The leakage inductance of the RIIT is used to replace the separate resonant inductors and compensate the *LCC* tank. The magnetizing current does not significantly reduce overall efficiency.

According to (3) and the energy conservation law, one can obtain the input current for #*i* inverter, $I_{{\rm in}\,i}$ (i = 2, 3, …, n)

$$I_{{\rm in}i}=2\sqrt{2}I_{\rm inv}\sin\alpha_i/(\pi n_i).\tag{18}$$

The transferred power of each inverter can be expressed as

$$P_{{\rm in}i}=I_{{\rm in}i}V_{\rm bus}=2\sqrt{2}I_{\rm inv}V_{\rm bus}\sin\alpha_i/(\pi n_i).\tag{19}$$

The power ratio of #*i* and #*j* inverters can be obtained as

$$P_{{\rm in}i}/P_{{\rm in}j}=n_j\sin\alpha_i/(n_i\sin\alpha_j),\ \alpha_j\neq 0.\tag{20}$$

Therefore, the power distribution among inverters can be easily controlled by regulating the phase angles.

To reduce the circulating current, the *LCC–LCC* WPT system operates at the resonant state and the basic equations are shown in the appendix. According to (45) and (46) in the appendix, the apparent power transferred through the coupling coils can be calculated as

$$\mathbf{S_{coil}}=j\omega M\mathbf{I_{ga}}\mathbf{I_{va}}=M\mathbf{V_{inv}}\mathbf{V_{rec}}/(j\omega L_{\rm r}L_{\rm f\_va}).\tag{21}$$

Since the phase angle between $\mathbf{V_{inv}}$ and $\mathbf{V_{rec}}$ is 90° at the resonance point, one can obtain the output power $P_{\rm o}$ as follows:

$$P_{\rm o}\approx MV_{\rm inv}V_{\rm rec}/(\omega L_{\rm r}L_{\rm f\_va}).\tag{22}$$

It is seen that $L_{\rm r}$ has a significant influence on the output power. The number of the RIITs can be varied according to the specifications, but the total leakage inductance is fixed.

According to the Fourier transform theory and FHA [21], $V_{\rm rec}$ can be obtained as

$$V_{\rm rec}=2\sqrt{2}V_{\rm bat}/\pi.\tag{23}$$

The output power of the proposed system can be derived as (24) by combining (11)–(22)

$$P_{\rm o}\approx\frac{8\left([0.25{\rm sgn}(x)+0.75]\sin\alpha_{1{\rm eq}}+\sum_{i=2}^{n}\sin\alpha_i/n_i\right)MV_{\rm bus}V_{\rm bat}}{\pi^2\omega L_{\rm r}L_{\rm f\_va}}.\tag{24}$$

The maximum power transferred by #*i* inverter is defined as $P_{i\_\max}$ where $\alpha_i=90°$. Since #1 inverter is directly connected to the resonant tank, n_1 can be regarded as 1. $P_{1\_\max}$ is different from $P_{i\_\max}$ when $n_i\neq 1$. According to (24), when $\alpha_{1{\rm eq}}=90°$ and $x=1$, $P_{1\_\max}$ can be approximately derived as

$$P_{1\_\max}=8MV_{\rm bus}V_{\rm bat}/(\pi^2\omega L_{\rm r}L_{\rm f\_va}).\tag{25}$$

By combining (2), (20), and (25), the relationship between $P_{1\_\max}$ and $P_{i\_\max}$ is given as

$$P_{i\_\max}=P_{1\_\max}/n_i=8kV_{\rm bus}V_{\rm bat}\sqrt{L_{\rm ga}L_{\rm va}}/(\pi^2 n_i\omega L_{\rm r}L_{\rm f\_va}).\tag{26}$$

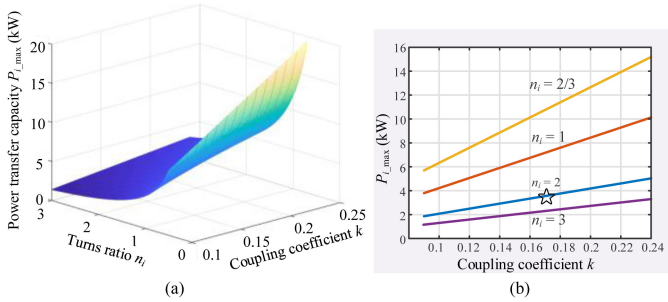

Fig. 10. Power transfer capacity of #*i* inverter $P_{i\_\max}$ with respect to coupling coefficient k and turns ratio n_i where $V_{\rm bus}$ = 400 V, $V_{\rm bat}$ = 800 V, $L_{\rm r}$ = 20 μH, $L_{\rm f\_va}$ = 35.5 μH, $L_{\rm ga}$ = 39 μH, $L_{\rm va}$ = 96 μH. (a) 3D view. (b) 2D view.

Fig. 10 shows the calculated $P_{i\_\max}$ with respect to k and n_i. It is seen that $P_{i\_\max}$ increases with the increase of k, whereas decreases with the increase of n_i.

By combining (24) and (25), the power gain $G_{\rm p}$ is defined as follows:

$$\begin{aligned}G_{\rm p}&=P_{\rm o}/P_{1\_\max}\\&=[0.25{\rm sgn}(x)+0.75]\sin\alpha_{1{\rm eq}}+\sum_{i=2}^{n}\sin\alpha_i/n_i\\&=\pi G_{\rm dc-ac}/(2\sqrt{2}).\end{aligned}\tag{27}$$

The essential requirement for the wide output power regulation range is to achieve a wide dc–ac voltage gain $G_{\rm dc\text{-}ac}$. The power rating of the proposed RIIT-MI WPT system can be easily improved by increasing the number of parallel inverters n. Furthermore, the operating mode x, phase angle α_i, duty cycle D_1, and turns ratio n_i can also be used to obtain the desired power and voltage gain. For example, if the maximum output power is 14 kW at $k=0.17$ and $n=3$, $P_{1\_\max}$ is 7.0 kW and $G_{\rm p}$ is around 2. Thus, n_2 and n_3 can be 2 where $P_{2\_\max}=P_{3\_\max}=0.5P_{1\_\max}=3.5$ kW, corresponding to the star point labelled in Fig. 10(b).

B. Autonomous Current Sharing

Without proper current sharing, the current stress may be imposed on particular inverters which could result in increased losses and device damage under high power applications. However, the proposed RIIT-MI topology can achieve current sharing autonomously.

Without loss of generality, we take the current sharing analysis between two neighboring inverters as an example. Fig. 11(a) shows the equivalent circuit of two RIITs. $i_{{\rm m}i}$, $i_{{\rm p}i}$, and $i_{{\rm s}i}$ are the magnetizing current, primary current, and secondary

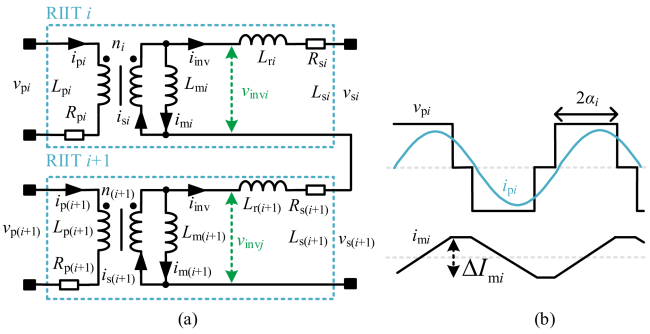

Fig. 11. Current sharing between two neighboring RIITs. (a) Equivalent circuit. (b) Typical waveform of $i_{\mathrm{m}i}$.

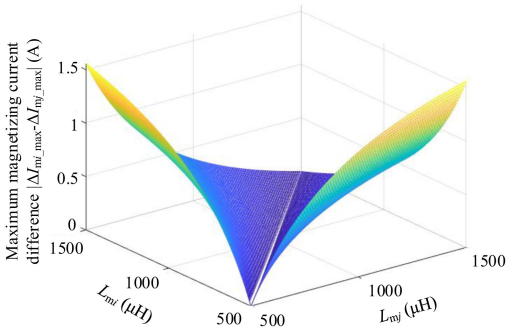

Fig. 12. Magnetizing current difference $|\Delta I_{\mathrm{m}i\_\max}$-$\Delta I_{\mathrm{m}j\_\max}|$ with respect to $L_{\mathrm{m}i}$ and $L_{\mathrm{m}j}$ where $f = 85.5$ kHz, $n_i = 2$, and $V_{\mathrm{bus}} = 400$ V.

current, respectively. $R_{\mathrm{p}i}$ and $R_{\mathrm{s}i}$ are the respective primary and secondary parasitic resistances of #*i* RIIT. $L_{\mathrm{p}i}$, $L_{\mathrm{s}i}$, $L_{\mathrm{r}i}$, $L_{\mathrm{m}i}$, and k_i are the primary and secondary self-inductance, leakage inductance, magnetizing inductance, and coupling coefficient of #*i* RIIT, respectively. Their relationships can be expressed as

$$L_{\mathrm{s}i} = L_{\mathrm{r}i} + L_{\mathrm{m}i} \tag{28}$$

$$L_{\mathrm{r}i} = (1 - k_i^2)L_{\mathrm{s}i}. \tag{29}$$

According to Kirchhoff's current law, one can obtain

$$i_{\mathrm{p}i} = (i_{\mathrm{inv}} + i_{\mathrm{m}i})/n_i. \tag{30}$$

The turns ratios of #2 $\sim$ #*n* RIITs are set to be identical as mentioned in (14). Therefore, the current difference between two RIITs is determined by $i_{\mathrm{m}i}$, which can be expressed as

$$v_{\mathrm{inv}i} = v_{\mathrm{p}i}/n_i = L_{\mathrm{m}i}di_{\mathrm{m}i}/dt. \tag{31}$$

Fig. 11(b) shows the waveform of $i_{\mathrm{m}i}$. The current difference becomes largest when one inverter operates at the FB-PSC scheme with 90° phase shift angle and another inverter operates at the BPC scheme. According to (31), one can obtain the maximum peak-to-peak value of the magnetizing current as

$$\Delta I_{\mathrm{m}i\_\max} = V_{\mathrm{bus}}/(2fn_iL_{\mathrm{m}i}). \tag{32}$$

It can be inferred from (32) that the current sharing performance is determined by the applied voltage V_{bus}, the operating frequency f, the turns ratio n_i, and the magnetizing inductance of the transformer $L_{\mathrm{m}i}$. In practice, the electrical parameters especially $L_{\mathrm{m}i}$ may be different due to the manufacturing accuracy. Fig. 12 shows the magnetizing current difference between two RIITs. Even if the magnetizing inductance differs by a factor of three, $|\Delta I_{\mathrm{m}i\_\max}$-$\Delta I_{\mathrm{m}j\_\max}|$ is still less than 1.5 A. Typically, $\Delta I_{\mathrm{m}i\_\max}$ is 1.2 A when $L_{\mathrm{m}i} = 1$ mH. Thus, the magnetizing current difference can be neglected at heavy loading. The inverting current of #1 inverter is i_{inv} and the inverting currents of #2 $\sim$ #*n* inverters are approximately equal to i_{inv}/n_i, i.e., $0.5i_{\mathrm{inv}}$ when $n_i = 2$. Since current sharing among different RIITs at various operation conditions can be achieved autonomously, the control complexity of the multiple inverters is greatly reduced.

C. Soft Switching Realization

The turn-off energy of a SiC MOSFET is much smaller than its turn-on energy. In addition, the parasitic output capacitance of semiconductors holds the voltage around zero during the transition which further reduces the turn-off switching loss. Thus, the focus of this article has been placed on the ZVS on.

Although FHA is accurate for main power transfer, high-order harmonics of $i_{\mathrm{p}i}$ should be considered when analyzing the switching conditions of the inverters.

Since the *LCC* resonant tank has a strong filtering effect for the high-order harmonics, the interaction of high-order harmonics between the GA and the VA can be neglected [27]. Then, according to the Fourier analysis, one can obtain the $(2m{+}1)$th order current $\mathbf{I}_{\mathrm{inv\_}(2m+1)\mathrm{th}}$ as

$$\begin{aligned}\mathbf{I}_{\mathrm{inv\_}(2m+1)\mathrm{th}} &\approx \frac{(2m{+}1)\mathbf{V}_{\mathrm{inv\_}(2m+1)\mathrm{th}}}{j((2m{+}1)^2-1)\omega L_{\mathrm{r}}} \\ &= \frac{\mathbf{V}_{\mathrm{inv}}}{j((2m{+}1)^2-1)\omega L_{\mathrm{r}}}.\end{aligned} \tag{33}$$

$\mathbf{I}_{\mathrm{inv\_}(2m+1)\mathrm{th}}$ lags $\mathbf{V}_{\mathrm{inv}}$ by 90° which increases the turn-off current and benefits the ZVS operation. Thus, the value of i_{inv} at the rising edge of v_{inv}, i.e., the turn-off current of #1 inverter $I_{\mathrm{OFF\_1}}$, can be obtained as

$$\begin{aligned}I_{\mathrm{OFF\_1}} &= -\sum_{m=1}^{\infty}\sqrt{2}I_{\mathrm{inv\_}(2m+1)\mathrm{th}} \\ &\approx -\sqrt{2}\sum_{m=1}^{\infty}\frac{V_{\mathrm{inv}}}{[(2m{+}1)^2-1]\omega L_{\mathrm{r}}} = -\frac{\sqrt{2}V_{\mathrm{inv}}}{4\omega L_{\mathrm{r}}}.\end{aligned} \tag{34}$$

Fig. 13 shows the waveforms of the inverting voltage and harmonic currents of #*i* inverter. The magnetizing current also increases the turn-off current, which reaches its negative peak value when α_i is 90°. Thus, one can obtain the turn-off current $I_{\mathrm{OFF\_}i}$ as (35) according to (30)

$$\begin{aligned}I_{\mathrm{OFF\_}i} &= -\frac{I_{\mathrm{OFF\_1}}}{n_i} - \frac{\Delta I_{\mathrm{m}i\_\max}}{2n_i} \\ &= -\left(\frac{\sqrt{2}V_{\mathrm{inv}}}{4n_i\omega L_{\mathrm{r}}} + \frac{V_{\mathrm{bus}}}{4fn_i^2L_{\mathrm{m}i}}\right).\end{aligned} \tag{35}$$

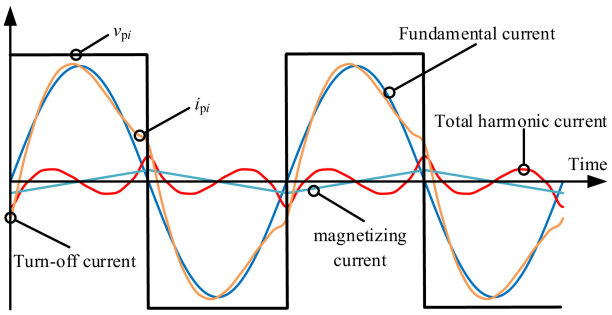

Fig. 13. Waveforms of the inverting voltage and harmonic currents of #*i* inverter.

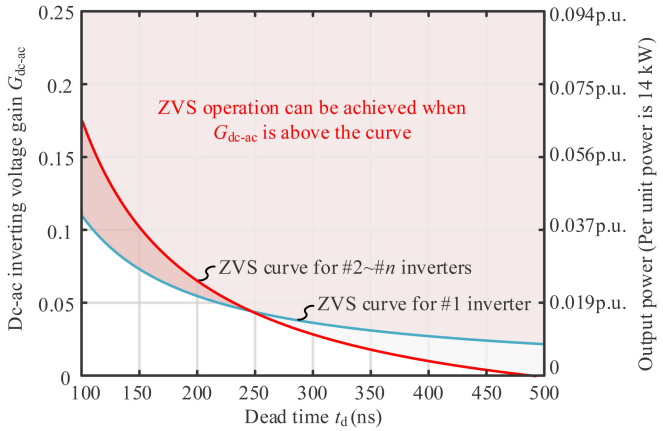

Fig. 14. ZVS region with respect to the dead time $t_{\rm d}$ where $V_{\rm bus} = 400$ V, $V_{\rm bus} = 800$ V, $L_{\rm r} = 20$ μH, $L_{\rm f\_va} = 35.5$ μH, $L_{\rm ga} = 39$ μH, $L_{\rm va} = 96$ μH, $k = 0.17$, $f = 85.5$ kHz, $C_{\rm OSSQ} = 180$ pF (C3M0021120K), $L_{{\rm m}i} = 1$ mH, $n_i = 2$.

The equivalent output capacitance of the switch, $C_{\rm OSSQ}$, should be fully charged or discharged by the turn-OFF current during the dead time $t_{\rm d}$. According to [28], the ZVS operation can be achieved when (36) is satisfied

$$\begin{cases} \frac{\sqrt{2}V_{\rm inv}}{4\omega L_{\rm r}} \geq \frac{2C_{\rm OSSQ}V_{\rm bus}}{t_{\rm d}}, & \text{ZVS for } \#1 \text{ inverter} \\ \frac{\sqrt{2}V_{\rm inv}}{4n_i\omega L_{\rm r}} + \frac{V_{\rm bus}}{4fn_i^2 L_{{\rm m}i}} \geq \frac{2C_{\rm OSSQ}V_{\rm bus}}{t_{\rm d}}, & \text{ZVS for } \#2 \sim \#n \text{ inverter} \end{cases}. \tag{36}$$

By combining (36) with (12), one can finally derive the ZVS region as

$$\begin{cases} G_{\rm dc-ac} \geq \frac{4\sqrt{2}\omega L_{\rm r}C_{\rm OSSQ}}{t_{\rm d}}, & \text{ZVS for } \#1 \text{ inverter} \\ G_{\rm dc-ac} \geq \frac{4\sqrt{2}n_i\omega L_{\rm r}C_{\rm OSSQ}}{t_{\rm d}} \\ \quad -\frac{\omega L_{\rm r}}{\sqrt{2}n_i f L_{{\rm m}i}}, & \text{ZVS for } \#2 \sim \#n \text{ inverter} \end{cases}. \tag{37}$$

The operating modes of the FB-PSC and HB-DCC schemes under ZVS operation have been presented in Figs. 6 and 8, respectively. It can be inferred from (37) that a bigger $t_{\rm d}$, a smaller $L_{\rm r}$, and a smaller $C_{\rm OSSQ}$ contribute to a smaller $G_{\rm dc\_ac}$, which facilitates the ZVS operation of the inverters. To make it more intuitive, Fig. 14 shows the ZVS region with respect to the dead time $t_{\rm d}$. $C_{\rm OSSQ}$ can be fully charged or discharged when $G_{\rm dc\_ac}$ is in the ZVS region. Taking $t_{\rm d} = 300$ ns as an example, #2 $\sim$ #*n* inverters operate at the FB-PSC scheme with 90°, i.e.,

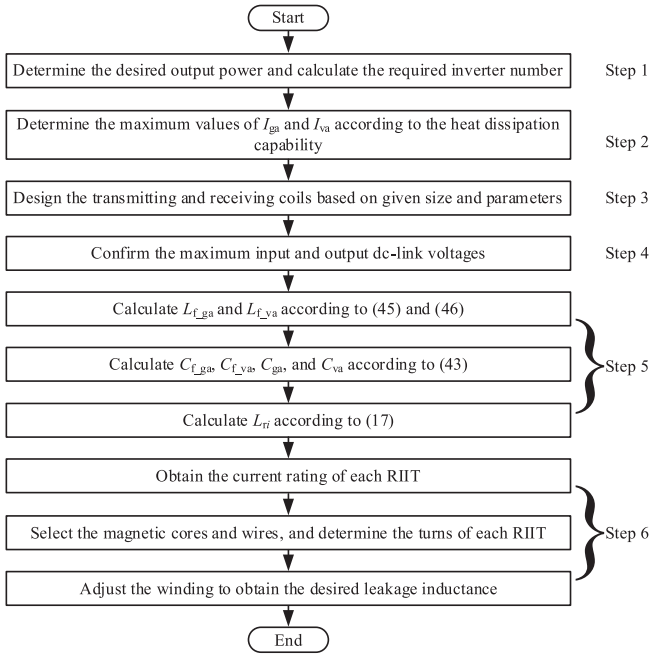

Fig. 15. Design procedure of the proposed system.

$G_{\rm dc\_ac}$ is greater than 0.5 which means ZVS operation can be achieved. The ZVS requirement for the HB-DCC scheme is that $G_{\rm dc\_ac}$ should be greater than 0.0365, i.e., $D_1 \geq 2.6\%$ or $P_{\rm o} \geq 0.014$ p.u. (per unit power is 14 kW). Thus, the proposed hybrid scheme helps to achieve a wide ZVS operation range for all the inverters.

D. Design Procedure and Considerations

This section presents the design procedure and serval considerations based on a 14-kW RIIT-MI WPT system.

Fig. 15 shows the design procedure for the proposed system, which can be roughly divided into six steps.

Step 1) The operating frequency is set at 85.5 kHz according to SAE J2954. The desired output power is given according to the application scenario. The power rating of each inverter is determined and then one can calculate the required inverter number.

Step 2) The maximum transmitting and receiving currents are determined according to the heat dissipation capability of the system. For example, the maximum values of $I_{\rm ga}$ and $I_{\rm va}$ in this article are 65 and 45 Arms, respectively.

Step 3) The transmitting and receiving coils are designed according to the given size and required power.

Step 4) The input and output dc-link voltages should be given. For example, the maximum values of $V_{\rm bus}$ and $V_{\rm bat}$ of the proposed prototype are 500 and 915 V, respectively.

Step 5) The resonant parameters are calculated in this step. One can obtain the calculated $L_{\rm f\_ga}$ and $L_{\rm f\_va}$ as 20.6 and 35.5 μH according to (45) and (46). $C_{\rm f\_ga}$ and $C_{\rm f\_va}$ resonate with $L_{\rm f\_ga}$ and $L_{\rm f\_va}$, respectively. $C_{\rm ga}$ resonates with $C_{\rm f\_ga}$ and $L_{\rm ga}$, and $C_{\rm va}$ resonates with $C_{\rm f\_va}$ and $L_{\rm va}$, whose values can

be calculated based on (43). The leakage inductance of each RIIT L_{ri} is $L_r/(n\text{-}1)$ according to (17).

Step 6) The design of RIIT is implemented. There are several magnetic integration methods for the resonant inductor. One can apply an air gap to the transformer which is widely used in the *LLC* converter. The required leakage inductance can be obtained by adjusting the length of the air gap. Another method can be to use an additional magnetic core with air gap for the resonant inductor. The third is to adjust the position of windings. The required total leakage inductance is usually tens of microhenry in the *LCC–LCC* EV WPT system, which is feasible for integrating the leakage inductance into the transformer. The turns ratios of RIITs are 2 as analyzed in Section II-C and EE70B ferrite core is used. 14:7 is chosen as the turns of windings to obtain the desired L_{ri} and ensure that the magnetic flux density of the ferrite core is less than 0.2 T. Thus, a leakage inductance of 10.3 μH for one RIIT in this article can be easily obtained by the third magnetic integration method.

As analyzed in Section II, the proposed system has the advantage of modular design. The sizes of one inverter and one RIIT in this article are 0.9 and 0.25 L, respectively. Thus, the system size is approximately increased by 1.15 L for one more module rated at 3.5 kW. In addition, the expression for a higher power rating has been derived in (24). Since $V_{\rm bus}$ and $V_{\rm bat}$ are determined by the application scenario, one can improve the system power rating by increasing the number of the inverters and rectifiers when $I_{\rm ga}$ and $I_{\rm va}$ are within the designed range. $I_{\rm ga\_max}$ and $I_{\rm va\_max}$ represent the maximum values of $I_{\rm ga}$ and $I_{\rm va}$. By combining (11) and (45), one can calculate $I_{\rm ga\_max}$ as

$$I_{\rm ga\_max} = 2\sqrt{2}\left(1+\sum_{i=2}^{n}1/n_i\right)V_{\rm bus}/\left(\pi\omega\sum_{i=2}^{n}L_{{\rm r}i}\right). \quad (38)$$

In practice, the maximum power transfer capacity $P_{\rm max}$ is determined by M, $I_{\rm ga\_max}$, and $I_{\rm va\_max}$ according to (21)

$$P_{\rm max} \approx \omega M I_{\rm ga\_max} I_{\rm va\_max}. \quad (39)$$

To obtain a higher power rating, one should increase M, $I_{\rm ga\_max}$, and $I_{\rm va\_max}$ which can be realized by increasing the turns of the coils and improving the heat dissipation capability.

The current stress of each converter can be decreased by increasing the number of inverters and rectifier diodes. To ensure $I_{\rm ga\_max}$ within the design range and avoid the thermal problem, the total leakage inductance $L_{\rm r}$ should increase with n. According to (38), the leakage inductance of each RIIT L_{ri} with respect to $I_{\rm ga\_max}$ is derived as follows where the same RIITs are used for all inverters with turns ratios of 2

$$L_{ri} = \frac{2\sqrt{2}V_{\rm bus}}{\pi\omega I_{\rm ga\_max}}\left(\frac{1}{n-1}+0.5\right), n \geq 2. \quad (40)$$

It can be inferred that L_{ri} slightly decreases with the increase of n. Since the magnetizing inductance of the RIIT is much larger than L_{ri}, the change of the coupling coefficient is very small and ignorable.

It should be noted that there are several tradeoffs when designing the system. The introduction of a water-cooling system can enable the integration of a high-power coil in a small VA. However, it increases the cost compared to an air-cooled system. The resonant inductors are integrated with the proposed RIIT, whose total size, weight, cost, and power losses can be smaller than that of separate transformers and inductors. This increases the accuracy required by the RIIT and poses more challenges for the transformer design. A higher $L_{{\rm m}i}$ corresponds to a smaller magnetic core loss and a smaller current difference between different RIITs as analyzed in Section III-B. However, it requires more turns of windings which increase the size and copper loss of the RIIT.

Fig. 16. A 14-kW RIIT-MI *LCC–LCC* WPT prototype.

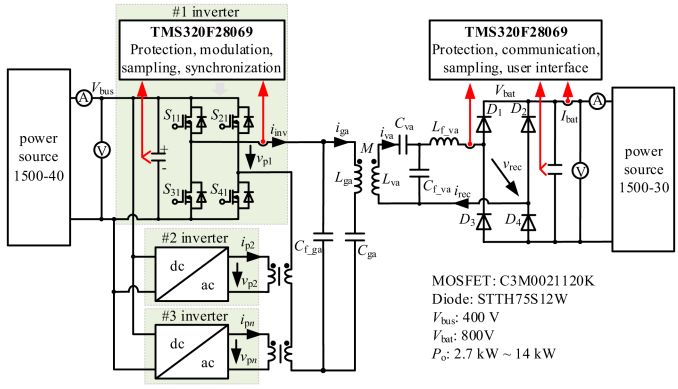

Fig. 17. Schematic of the lab prototype.

IV. Experimental Verification

A 14-kW *LCC-LCC* WPT prototype was built to verify the proposed RIIT-MI topology. Fig. 16 shows the experimental setup and Fig. 17 shows the schematic of the prototype. Three parallel inverters are controlled by three independent digital signal processors (TMS320F28069). #1 inverter acts as the master which generates a square-wave synchronization signal. #2 and

TABLE III
KEY PARAMETERS OF PROPOSED PROTOTYPE

Symbol	Parameter	Value
P_o	Output power	14 kW
V_{bat}	Output voltage	800 V
V_{bus}	Input voltage	400 V
f	Operating frequency	85.5 kHz
$C_{f\ ga}$	Primary filtering capacitor	168 nF
C_{ga}	Resonant capacitor	175 nF
L_{ga}	Self-inductance of transmitting coil	39μH
L_{va}	Self-inductance of receiving coil	96 μH
C_{va}	Resonant capacitor	55 nF
$C_{f\ va}$	Secondary filtering capacitor	105 nF
$L_{f\ va}$	Secondary filtering inductor	35.5 μH
n	Number of inverters	3
n_{p2}:n_{s2}, n_{p3}:n_{s3}	Turns ratios of RIITs	14:7
L_{r2}/ L_{r3}	Leakage inductance of RIIT	9.4 μH/10.3 μH

TABLE IV
COMPARISON BETWEEN SEPARATE SOLUTION AND PROPOSED RIITS

	Separate solution	Proposed RIITs
Number of transformers	2	2
Number of inductors	1	0
Size	Large	Medium
Weight	1.3 kg (transformers) + 0.72 kg (inductors)	1.3 kg (transformers)
Total power loss	Slightly higher	Small

#3 inverters are the slavers. The inverting voltages of #1–#3 inverters are in phase with each other. Each inverter consists of four SiC MOSFETs (C3M0021120Ks) and the rectifier diodes are STTH75S12Ws. A water-cooling system is used on the VA side. Table III lists the key parameters of the proposed system. Two 18-kW regenerative power sources IT6018C-1500-40/IT6018C-1500-30 are utilized as the input voltage and the output load, where V_{bus} and V_{bat} are set at 400 and 800 V, respectively. Tektronix MSO56 5-BW-1000 six-channel oscilloscope is used to record the experimental waveforms. The sizes of transmitting and receiving coils are 80 cm × 70 cm × 6 cm and 37 cm × 37 cm × 6 cm, respectively.

Two RIITs are used, whose L_m and k are 1488 μH and 0.986, respectively. The total leakage inductance L_r is about 19.7 μH. Table IV further compares the separate resonant inductors and transformers used in a 10-kW WPT system and the RIITs used in the proposed system. The total size, weight, and power loss of the RIITs are better than that of a separate solution.

The selection of dead time depends on soft switching requirements and the characteristics of the MOSFET. The rise time, fall time, turn-on delay time, and turn-off delay time of C3M0021120K are 33, 14, 13, and 23 ns, respectively. As analyzed in Fig. 14, a wide soft switching region can be obtained with a dead time of 300 ns. Therefore, the dead time is set to be 300 ns and remains unchanged for different loads.

A. Autonomous Current Sharing

Fig. 18 shows the experimental results of the autonomous current sharing under various conditions. #1 inverter is directly connected to the resonant tank where n_1 is regarded as 1. Both the turns ratios of #2 and #3 inverters are 2 to ensure a large α_{i_min} as discussed in Section II-C. Thus, i_{inv} is double of i_{p2} and i_{p3} in this experiment. In Fig. 18(a), #1 inverter operates at the HB-DCC scheme with a duty cycle of 50%, whereas #2 and #3 inverters operate at the BPC scheme. The current difference between I_{p2} and I_{p3} is 0.04 Arms. In Fig. 18(b), #1 inverter operates at the HB-DCC scheme with a duty cycle of 50%. #2 inverter operates at the FB-PSC scheme with a phase angle of 90° and #3 inverter operates at the BPC scheme. The current difference between I_{p2} and I_{p3} is 0.03 Arms. In Fig. 18(c), #1 inverter operates at the HB-DCC scheme with a duty cycle of 50%, whereas #2 and #3 inverters operate at the FB-PSC scheme with a phase angle of 90°. The current difference between I_{p2} and I_{p3} is 0.05 Arms. In Fig. 18(d), all these inverters operate at the FB-PSC scheme with a phase angle of 90°. The current difference between I_{p2} and I_{p3} is 0.27 Arms. The currents flowing through #2 and #3 inverters are almost the same even under these harsh operation conditions, which confirms that the proposed RIIT-MI topology has an inherent autonomous current sharing characteristic as discussed in Section III-B.

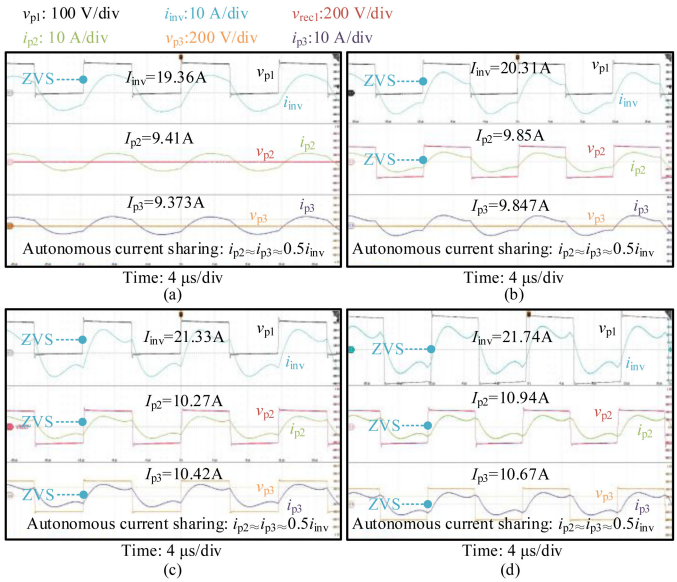

Fig. 18. Autonomous current sharing at different conditions. (a) #1 inverter operates at the HB-DCC scheme and #2 and #3 inverters operate at the BPC scheme, where $D_1 = 50\%$; (b) #1, #2, and #3 inverters operate at the HB-DCC scheme, the FB-PSC scheme, and the BPC scheme, respectively, where $D_1 = 50\%$ and $\alpha_2 = 90°$; (c) #1 inverter operates at the HB-DCC scheme and #2 and #3 inverters operate at the FB-PSC scheme, where $D_1 = 50\%$ and $\alpha_2 = \alpha_3 = 90°$; (d) #1, #2, and #3 inverters operate at the FB-PSC scheme where $\alpha_1 = \alpha_2 = \alpha_3 = 90°$.

B. Hybrid Modulation Scheme

Fig. 19 shows the various operating modes of the proposed hybrid modulation scheme. The power transfer distance is 18 cm and the coupling coefficient is 0.17. The calculated power transfer capacity of #1 and the other two inverters are 7.0 and 3.5 kW, respectively. The maximum calculated power transfer capacity agrees well with the maximum experimental power of 14 kW. In Fig. 19(a) and (b), all the inverters operate at the FB-PSC scheme and the phase angle of #1 inverter decreases from 90° to 75°. In Fig. 19(c)–(e), #1 inverter operates at the

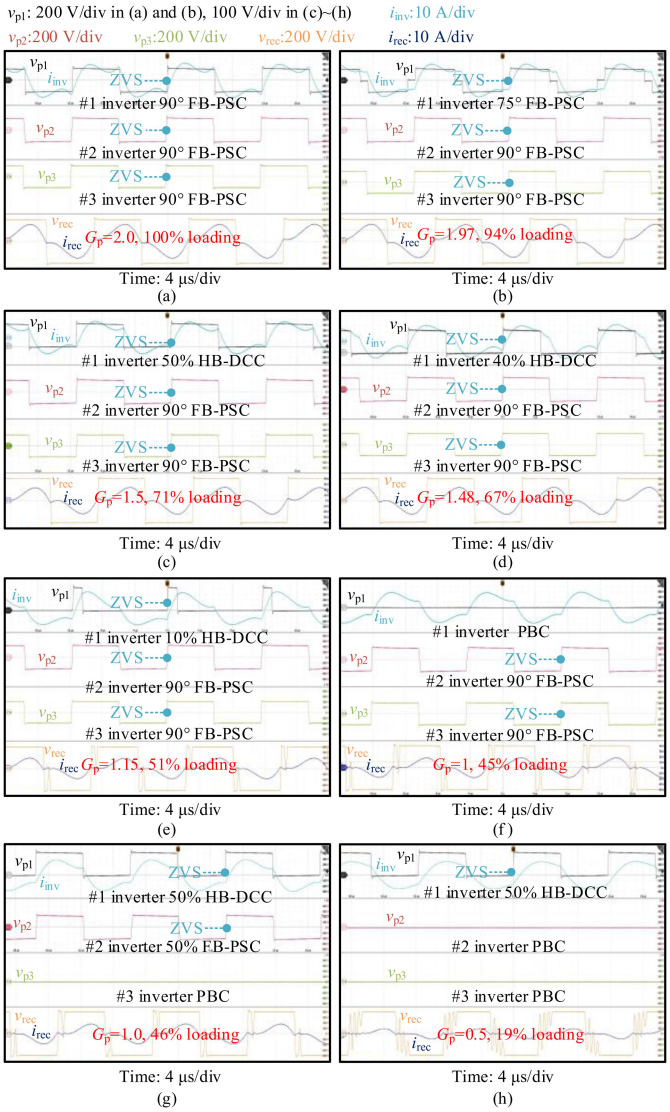

Fig. 19. Typical waveforms of various operating modes of the proposed hybrid modulation scheme. (a) #1, #2, and #3 inverters operate at the FB-PSC scheme where $\alpha_1 = \alpha_2 = \alpha_3 = 90°$. (b) #1, #2, and #3 inverters operate at the FB-PSC scheme where $\alpha_1 = 75°$ and $\alpha_2 = \alpha_3 = 90°$. (c) #1 inverter operates at the HB-DCC scheme and #2 and #3 inverters operate at the FB-PSC scheme, where $D_1 = 50\%$ and $\alpha_2 = \alpha_3 = 90°$. (d) #1 inverter operates at the HB-DCC scheme and #2 and #3 inverters operate at the FB-PSC scheme where $D_1 = 40\%$ and $\alpha_2 = \alpha_3 = 90°$. (e) #1 inverter operates at the HB-DCC scheme and #2 and #3 inverters operate at the FB-PSC scheme where $D_1 = 10\%$ and $\alpha_2 = \alpha_3 = 90°$. (f) #1 inverter operates at the BPC scheme and #2 and #3 inverters operate at the FB-PSC scheme where $\alpha_2 = \alpha_3 = 90°$. (g) #1, #2, and #3 inverters operate at the HB-DCC scheme, the FB-PSC scheme, and the BPC scheme, respectively, where $D_1 = 50\%$ and $\alpha_2 = 90°$. (h) #1 inverter operates at the HB-DCC scheme and #2 and #3 inverters operate at the BPC scheme, where $D_1 = 50\%$.

HB-DCC scheme and their duty cycles are 50%, 40%, and 10%, respectively. In Fig. 19(f), #1 inverter operates at the BPC scheme. In Fig. 19(g), #1 inverter operates at the HB-DCC scheme with 50% duty cycle, whereas #2 and #3 inverters operate at the FB-PSC scheme and the BPC scheme, respectively. In Fig. 19(h), #1 inverter operates at the HB-DCC scheme and the other inverters operate at the BPC scheme. For a particular voltage gain of the proposed hybrid modulation scheme, there is

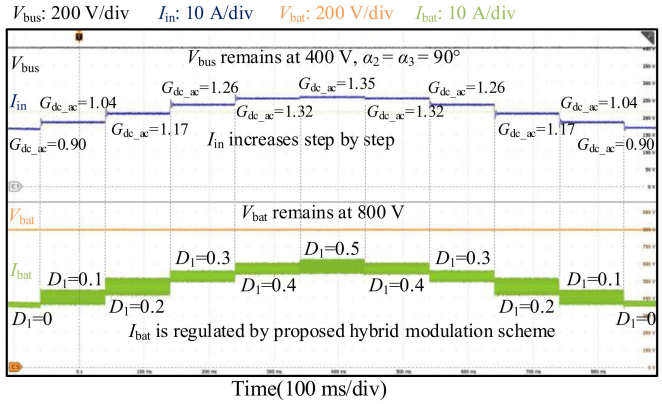

Fig. 20. Power steps by proposed hybrid modulation scheme where $V_{bus} = 400$ V and $V_{bat} = 800$ V. #1 inverter operates at the HB-DCC scheme, and #2 and #3 inverters operate at the FB-PSC scheme where $\alpha_2 = \alpha_3 = 90°$. D_1 changes from 0 to 50% and the output power changes from 6.2 to 9.9 kW.

one combination of operating modes, phase angles α_i, and duty cycle D_1. Given a voltage gain, the operating modes, the phase angles, and the duty cycle can be determined according to Fig. 8. Theoretically, the output power of Fig. 19(f) and (g) should be the same since they are the boundary of two modes. However, due to the small system parameter variation, there exists a 1% experimental power discrepancy.

With the proposed hybrid modulation scheme, all the inverters can operate at optimal conditions, ensuring that the zero-crossing point of the resonant current always lags the voltage at the transitions. As can be seen from Fig. 19, the ZVS operation can be achieved by all the MOSFETs, which can reduce the switching losses and the electromagnetic interferences.

Fig. 20 shows the experimental result of the wide-range power regulation. The input and output voltages remain at 400 and 800 V, respectively. #2 and #3 inverters operate at the FB-PSC scheme with a phase angle of 90°. D_1 increases from 0 to 50% by a step of 10% and then it decreases from 50% to 0. According to the definition in (12), $G_{\text{dc-ac}}$ changes from 0.90 to 1.35. The input and output current increases with the increase of D_1. The experimental output power ranges from 6.2 to 9.9 kW which agrees with the calculation based on (24).

Fig. 21 shows the dc–dc efficiency at various loading conditions. The power transfer efficiency increases with P_o and it is greater than 91% with an output power of ~6 kW. The achieved maximum efficiency is 93.5% at 14 kW. The main power losses are produced by the transmitting and receiving coils. A diode rectifier is used on the VA side and the output voltage is fixed at 800 V. Thus, the resonant current I_{va} remains around 40 Arms despite the power variations according to (46). When P_o is small, the power loss of the receiving coil accounts for a large portion of P_o which significantly reduces the dc–dc efficiency.

Fig. 22 shows the power loss breakdown at different power levels. The power losses of the GA coil, VA coil, and filters account for the major portion of the total power losses. The filters include differential and common-mode inductors, notch filters for interference reduction required by the auxiliary circuits such as foreign object detection. The balance of losses represents

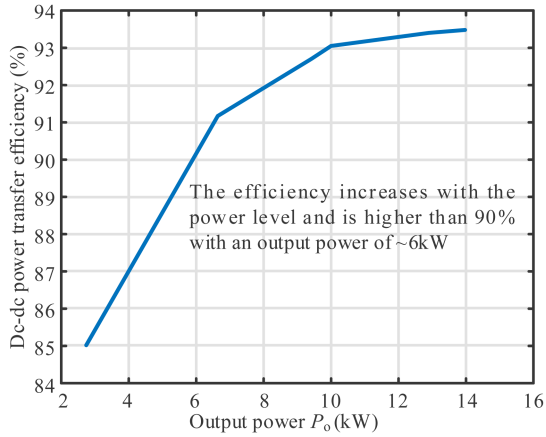

Fig. 21. DC–DC power transfer efficiency with respect to the output power P_o where $V_{bus} = 400$ V and $V_{bat} = 800$ V.

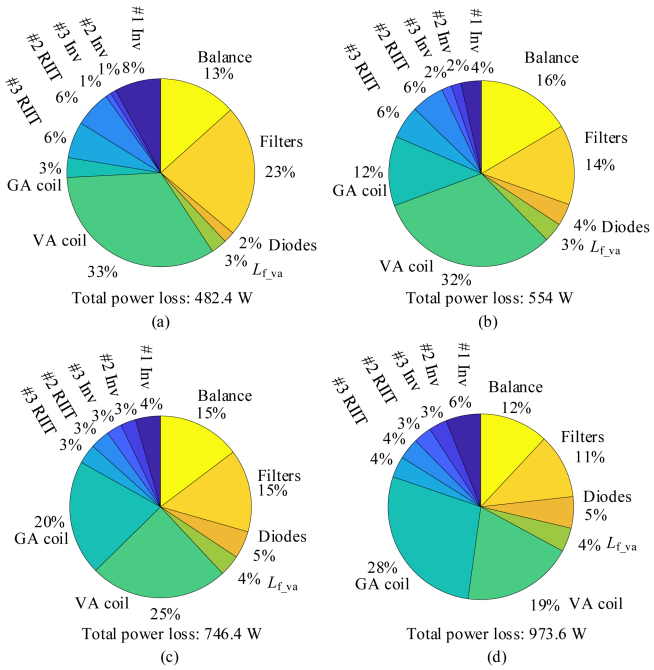

Fig. 22. Power loss breakdown at different power levels. (a) $P_o = 2.7$ kW. (b) $P_o = 6.3$ kW. (c) $P_o = 10$ kW. (d) $P_o = 14$ kW.

the power losses that are not easily measured in the connectors, filtering capacitors, metal housing, reverse recovery losses, etc. Due to the DPAS architecture, V_{inv} can be significantly increased and I_{inv} can remain unchanged at high power levels according to (44), which reduces the current stress of each inverter. Although diode rectifiers (instead of active rectifiers) can reduce the size of the VA, the loss of secondary side control means that a maximum efficiency tracking may not be implemented. As a result, the VA coil loss remains almost constant, which results in a lower efficiency at a low output power. The power loss of each inverter decreases with the decreasing output power. Although the proportion of power loss of #1 inverter is increased to 8% at 2.7 kW, the power loss is only 60% of that at 14 kW.

TABLE V
COMPARISON OF DIFFERENT SYSTEMS

Topology	Multi-cell		Multi-GA		Multi-inverter	
Ref.	[7]	[9]	[12]	[13]	[15]	This study
Wide power regulation range	NA	NA	NA	NA	√	√
Wide ZVS operation range	NA	NA	NA	×	NA	√
Autonomous current sharing	×	×	×	×	×	√
Modular design	√	√	√	√	√	√
Coupling coefficient	0.20	0.22	0.20	0.20	0.24	0.17
GA coil (cm^2)	35*95	42*42	93*59	90*70	40*40	80*70
VA coil (cm^2)	50*90	42*42	100*70	90*70	40*40	37*37
Power rating (kW)	50	0.2	38	12.5	3.2	14
Power density of VA (kW/L)	NA	0.022	NA	NA	NA	1.7
Dc-dc efficiency	95.2%	89.8%	89.31%	92.6%	93.5%	93.5%

The hybrid modulation scheme is proposed to obtain a wide-range power supply and achieve soft switching. This part provides the experimental study where the output power ranges from 2.7 kW to 14 kW, which confirms the operating mode analysis in Section II-B and the proposed hybrid modulation scheme in Section II-C.

C. Comparison and Discussions

As mentioned in Section I, there are various methods to improve the power transfer capacity of the WPT system including the multi-MOSFET, multi-module, multi-GA, and MI solutions. However, the current sharing, limited size, cross-coupling, and circulating current issues of these topologies are not easy to address.

Table V compares various high-power WPT topologies as shown in Fig. 1. According to the theoretical analysis in Section III-C, the ZVS operation can be obtained when the power ranges from 0.014 to 1 p.u. In the experiments, ZVS has been achieved by the proposed hybrid modulation scheme when the load changes from 0.2 to 1.0 p.u. Therefore, a wide power regulation range and wide ZVS operation range can be achieved simultaneously. The conventional dc–dc regulator can be removed and the system becomes more compact and efficient. In addition, autonomous current sharing among parallel inverters has been always achieved. Owing to the modular design, the power transfer capacity of the system can be easily increased by adding inverters, changing the turns ratio of the RIIT, increasing the bus voltage, etc. Therefore, the proposed RIIT-MI topology presents an efficient, cost-effective, flexible, and generalized solution for the high-power WPT system.

V. CONCLUSION

To improve the power transfer capacity and adapt to various power demands, this article proposed an RIIT-MI DPAS topology for the high-power EV WPT system. Based on this topology, a hybrid modulation scheme was proposed to achieve a wide power regulation range and ZVS operation by using primary continuous modulation schemes at a fixed frequency.

The proposed RIIT replaces the conventional resonant inductor of the GA and eliminates the conventional dc–dc regulator or active rectifier, which enables the system with fewer devices and lower cost. Current sharing among parallel inverters can be autonomously achieved, which reduces the control complexity. Furthermore, flexible power transfer with a wide ZVS operation range can be achieved by the proposed modulation scheme. A 14-kW experimental platform with a maximum dc–dc efficiency of 93.5% has been built and the effectiveness of the proposed technique has been validated.

APPENDIX A

The basic equations of the *LCC-LCC* WPT system will be presented in this section.

To simplify the derivation, different impedances have been defined as

$$\begin{aligned} &X_1 = \omega L_{\rm r} - \tfrac{1}{\omega C_{\rm f\_ga}}, X_2 = \omega L_{\rm ga} - \tfrac{1}{\omega C_{\rm ga}} \\ &X_3 = \omega L_{\rm va} - \tfrac{1}{\omega C_{\rm va}}, X_4 = \omega L_{\rm f\_va} - \tfrac{1}{\omega C_{\rm f\_va}} \\ &X_{\rm ga} = -\tfrac{1}{\omega C_{\rm f\_ga}}, X_{\rm va} = -\tfrac{1}{\omega C_{\rm f\_va}}, X_{\rm m} = \omega M. \end{aligned} \tag{41}$$

According to the circuit theory and Fig. 9, the following equation can be deduced where the bold letters represent the phasors of these variables:

$$\begin{bmatrix} \mathbf{V_{inv}} \\ \mathbf{0} \\ \mathbf{0} \\ \mathbf{V_{rec}} \end{bmatrix} = \begin{bmatrix} jX_1 & -jX_{\rm ga} & 0 & 0 \\ -jX_{\rm ga} & jX_2 + R_{\rm ga} & -jX_{\rm m} & 0 \\ 0 & -jX_{\rm m} & jX_3 + R_{\rm va} & -jX_{\rm va} \\ 0 & 0 & jX_{\rm va} & jX_4 \end{bmatrix} \begin{bmatrix} \mathbf{I_{inv}} \\ \mathbf{I_{ga}} \\ \mathbf{I_{va}} \\ \mathbf{I_{rec}} \end{bmatrix}. \tag{42}$$

To ensure a resistive load and minimum circulating current, the compensation circuits of GA and VA are designed at the resonant point [27]. Then, one can obtain

$$\begin{aligned} &\tfrac{1}{\omega C_{\rm f\_ga}} = \omega L_{\rm ga} - \tfrac{1}{\omega C_{\rm ga}}, \omega L_{\rm r} = \tfrac{1}{\omega C_{\rm f\_ga}} \\ &\tfrac{1}{\omega C_{\rm f\_va}} = \omega L_{\rm va} - \tfrac{1}{\omega C_{\rm va}}, \omega L_{\rm f\_va} = \tfrac{1}{\omega C_{\rm f\_va}}. \end{aligned} \tag{43}$$

The parasitic resistances of coils are small and can be neglected. Different resonant currents are derived as

$$\mathbf{I_{inv}} = \frac{X_m \mathbf{V_{rec}}}{jX_{\rm ga}X_{\rm va}} \tag{44}$$

$$\mathbf{I_{ga}} = \frac{\mathbf{V_{inv}}}{jX_{\rm ga}} \tag{45}$$

$$\mathbf{I_{va}} = \frac{\mathbf{V_{rec}}}{jX_{\rm va}} \tag{46}$$

$$\mathbf{I_{rec}} = \frac{X_m \mathbf{V_{inv}}}{-jX_{\rm ga}X_{\rm va}}. \tag{47}$$

REFERENCES

[1] I. Aghabali, J. Bauman, P. J. Kollmeyer, Y. Wang, B. Bilgin, and A. Emadi, "800-V Electric vehicle powertrains: Review and analysis of benefits, challenges, and future trends," *IEEE Trans. Transp. Electrific.*, vol. 7, no. 3, pp. 927–948, Sep. 2021.

[2] "Wireless power transfer for light-duty plug-in/electric vehicles and alignment methodology," International Standard SAE J2954, 2019. [Online]. Available: https://www.sae.org/standards/content/j2954_201904/

[3] Y. Chen, H. Zhang, C.-S. Shin, C.-H. Jo, S.-J. Park, and D.-H. Kim, "An efficiency optimization-based asymmetric tuning method of double-sided LCC compensated WPT system for electric vehicles," *IEEE Trans. Power Electron.*, vol. 35, no. 11, pp. 11475–11487, Nov. 2020.

[4] Y. Zhang, S. Chen, X. Li, and Y. Tang, "Design of high-power static wireless power transfer via magnetic induction: An overview," *CPSS Trans. Power Electron. Appl.*, vol. 6, no. 4, pp. 281–297, Dec. 2021.

[5] R. Bosshard, "Multi-objective optimization of inductive power transfer systems for EV charging," Ph.D. dissertation, ETHZ, Zurich, 2015.

[6] Y. Wen, Y. Yang, and Y. Gao, "Active gate driver for improving current sharing performance of paralleled high-power SiC MOSFET modules," *IEEE Trans. Power Electron.*, vol. 36, no. 2, pp. 1491–1505, Feb. 2021.

[7] A. U. Ibrahim, W. Zhong, and M. D. Xu, "A 50-kW three-channel wireless power transfer system with low stray magnetic field," *IEEE Trans. Power Electron.*, vol. 36, no. 9, pp. 9941–9954, Sep. 2021.

[8] H. Zhang, C. Ma, and M. Liu, "Modularized and reconfigurable wireless power transfer: Architecture, modeling and analysis," in *Proc. IEEE PELS Workshop Emerg. Technol., Wireless Power Transfer*, Jun. 2021, pp. 1–6.

[9] W. Cai, H. Tang, D. Ma, and X. Liu, "Voltage control and current distribution for multiple-coil wireless power transfer system," in *Proc. IEEE Wireless Power Transfer Conf.*, 2019, pp. 548–552.

[10] J. H. Kim et al., "Development of 1-MW inductive power transfer system for a high-speed train," *IEEE Trans. Ind. Electron.*, vol. 62, no. 10, pp. 6242–6250, Oct. 2015.

[11] J. Pries, V. P. N. Galigekere, O. C. Onar, and G. Su, "A 50-kW three-phase wireless power transfer system using bipolar windings and series resonant networks for rotating magnetic fields," *IEEE Trans. Power Electron.*, vol. 35, no. 5, pp. 4500–4517, May 2020.

[12] H. Zhou et al., "Input-Series output-equivalent-parallel multi-inverter system for high-voltage and high-power wireless power transfer," *IEEE Trans. Power Electron.*, vol. 36, no. 1, pp. 228–238, Jan. 2021.

[13] Q. Deng et al., "Multi-Inverter phase-shifted control for IPT with overlapped transmitters," *IEEE Trans. Power Electron.*, vol. 36, no. 8, pp. 8799–8811, Aug. 2021.

[14] Y. Li, R. Mai, L. Lu, and Z. He, "Active and reactive currents decomposition-based control of angle and magnitude of current for a parallel multiinverter IPT system," *IEEE Trans. Power Electron.*, vol. 32, no. 2, pp. 1602–1614, Feb. 2017.

[15] H. He, Y. Liu, B. Wei, X. Wu, B. Jiang, and C. Wei, "Efficiency improvement for Multi-parallel inverters IPT system in wide power range," in *Proc. IEEE 1st Int. Power Electron. Appl. Symp.*, 2021, pp. 1–6.

[16] R. Bosshard, U. Iruretagoyena, and J. W. Kolar, "Comprehensive evaluation of rectangular and Double-D coil geometry for 50 kW/85 kHz IPT system," *IEEE J. Emerg. Sel. Topics Power Electron.*, vol. 4, no. 4, pp. 1406–1415, Dec. 2016.

[17] Y. Li et al., "Extension of ZVS region of series–series WPT systems by an auxiliary variable inductor for improving efficiency," *IEEE Trans. Power Electron.*, vol. 36, no. 7, pp. 7513–7525, Jul. 2021.

[18] Z. Guo, K. Sun, T.-F. Wu, and C. Li, "An improved modulation scheme of current-fed bidirectional DC–DC converters for loss reduction," *IEEE Trans. Power Electron.*, vol. 33, no. 5, pp. 4441–4457, May 2018.

[19] X. Zhang et al., "A control strategy for efficiency optimization and wide ZVS operation range in bidirectional inductive power transfer system," *IEEE Trans. Ind. Electron.*, vol. 66, no. 8, pp. 5958–5969, Aug. 2019.

[20] S. Ann and B. K. Lee, "Analysis of impedance tuning control and synchronous switching technique for a semibridgeless active rectifier in inductive power transfer systems for electric vehicles," *IEEE Trans. Power Electron.*, vol. 36, no. 8, pp. 8786–8798, Aug. 2021.

[21] X. Liu, T. Wang, X. Yang, and H. Tang, "Analysis of efficiency improvement in wireless power transfer system," *IET Power Electron,* vol. 11, no. 2, pp. 302–309, Feb. 2018.

[22] L. H. Chan, Y. Yang, and K.-W. E. Cheng, "Comparative studies on the primary-side frequency and phase shift control for series-series compensated inductive power transfer," in *Proc. 8th Int. Conf. Power Electron. Syst. Appl.*, Dec. 2020, pp. 1–5.

[23] U. D. Kavimandan, S. M. Mahajan, and C. W. Van Neste, "Analysis and demonstration of a dynamic ZVS angle control using a tuning capacitor in a wireless power transfer system," *IEEE J. Emerg. Sel. Topics Power Electron.*, vol. 9, no. 2, pp. 1876–1890, Apr. 2021.

[24] F. Gao, N. Mugwisi, and D. J. Rogers, "Average modeling of a dual-half-bridge converter modulated with three degrees of freedom," *IEEE Trans. Transp. Electrific.*, vol. 7, no. 3, pp. 1016–1030, Sep. 2021.

[25] Z. Hua, K. T. Chau, W. Han, W. Liu, and T. W. Ching, "Output-controllable efficiency-optimized wireless power transfer using hybrid modulation," *IEEE Trans. Ind. Electron.*, vol. 69, no. 5, pp. 4627–4636, May 2022.

[26] W. Inam, K. K. Afridi, and D. J. Perreault, "Variable frequency multiplier technique for high-efficiency conversion over a wide operating range," *IEEE J. Emerg. Sel. Topics Power Electron.*, vol. 4, no. 2, pp. 335–343, Jun. 2016.
[27] S. Li, W. Li, J. Deng, T. D. Nguyen, and C. C. Mi, "A double-sided LCC compensation network and its tuning method for wireless power transfer," *IEEE Trans. Veh. Technol.*, vol. 64, no. 6, pp. 2261–2273, Jun. 2015.
[28] Y. Zhang, X. Li, S. Chen, and Y. Tang, "Soft switching for strongly coupled wireless power transfer system with 90° dual-side phase shift," *IEEE Trans. Ind. Electron.*, vol. 69, no. 1, pp. 282–292, Jan. 2022.

Xin Liu (Member, IEEE) received the B.S. degree in electrical engineering from the Wuhan University, Wuhan, China, in 2015, and the Ph.D. degree in electrical engineering from the Shanghai Jiao Tong University, Shanghai, China, in 2019.

From Aug. 2019 to Aug. 2021, he was with Huawei Technologies Co., Ltd. Since September 2021, he has been with the Department of Electrical Engineering, Shanghai Jiao Tong University, as a postdoctoral researcher. His current research interests include wireless power transfer and solid-state transformers.

Fei Gao (Member, IEEE) received the Ph.D. degree in electrical engineering from the Power Electronics, Machines, and Control (PEMC) Research Group, University of Nottingham, Nottingham, U.K., in 2016.

From March 2010 to September 2012, he was with Jiangsu Electric Power Research Institute, State Grid Corporation of China, Nanjing, China. From 2016 to 2019, he was with the Department of Engineering Science, University of Oxford, Oxford, U.K., as a Postdoctoral Researcher. Since July 2019, he has been with Shanghai Jiao Tong University as an Associate Professor. His current research interests include microgrids, wireless power transfer, and more electric transportation systems.

Yiming Zhang (Senior Member, IEEE) received the B.S. and Ph.D. degrees in electrical engineering from Tsinghua University, Beijing, China, in 2011 and 2016, respectively.

He was a Postdoctoral Researcher with San Diego State University, San Diego, CA, USA, and a research fellow with the Nanyang Technological University, Singapore. He is currently a Full Professor with Fuzhou University, Fuzhou, China. He has authored 1 book from Springer, authored or co-authored more than 80 technical papers in journals and conference proceedings. His research interests include wireless power transfer and resonant converters.

Dr. Zhang was the recipient of the Outstanding Doctoral Dissertations of Tsinghua University in 2016. He was recognized as an Outstanding Reviewer for IEEE TRANSACTIONS ON POWER ELECTRONICS in 2019 and a Distinguished Reviewer for IEEE TRANSACTIONS ON INDUSTRIAL ELECTRONICS in 2020. He was a Topic Chair for IEEE Transportation Electrification Conference and Expo (ITEC) in 2018.

Muhammad Mansoor Khan (Member, IEEE) received the Ph.D. degree in control and automation engineering from the Department of Control Sciences, School of Electronics Information and Electrical Engineering, Shanghai Jiao Tong University, Shanghai, China, in 2005.

In 2005, he joined the Department of Electrical Engineering, School of Electronics Information and Electrical Engineering, Shanghai Jiao Tong University, where he is currently working as an Associate Professor. His research interests include power converters for renewable energy systems, power quality, hierarchical control of microgrids, plug-in electric vehicles, and energy storage technologies.

Yun Zhang (Senior Member, IEEE) was born in Jiangsu, China, in 1980. He received the B.S. and M.S. degrees from the Harbin University of Science and Technology, Harbin, China, in 2003 and 2006, respectively, and the Ph.D. degree from the Harbin Institute of Technology, Harbin, China, in 2010, all in electrical engineering.

In 2010, he joined as a Lecturer with the School of Electrical and Information Engineering, Tianjin University, Tianjin, China, where he is currently a Professor of power electronics. From 2016 to 2017, he was an Academic Visitor with the Power Electronics, Machines and Control Group, University of Nottingham, Nottingham, U.K. His current research interests include topologies, modulation, and control strategies of power converters for electric vehicles and microgrids.

Dr. Zhang is an Associate Editor for the *Journal of Power Electronics*.

Tianfeng Wang received the B.S. degree in electrical engineering from the Beijing Institute of Technology, Beijing, China, in 2015, the Ph.D. degree in electrical engineering from the Shanghai Jiao Tong University, Shanghai, China, in 2022.

From 2018 to 2020, he was a visiting graduate student with the University of Pittsburgh, Pittsburgh, PA, USA. Since April 2022, he has been with the Department of Electrical Engineering, Shanghai Jiao Tong University, Shanghai, China as a Postdoctoral Researcher. His current research interests include wireless power transfer and wireless communication.

Daniel J. Rogers (Senior Member, IEEE) received the M.Eng. and Ph.D. degrees in electrical and electronic engineering from Imperial College London, London, U.K., in 2007 and 2011, respectively.

He is an Associate Professor with the Department of Engineering Science, University of Oxford, Oxford, U.K. He conducts research in collaboration with industry and has been an investigator on U.K. EPSRC research projects in the areas of power electronics, grid-scale energy storage, and microgrids. His research interests include power electronics range from active control of transistor switching, to circuit and control system design, through to novel applications enabled by wide-bandgap devices.